Article

Twin Boundary Induced Grain Coarsening in Friction Stir Welding of Fine- and Ultra-Fine-Grained Commercially Pure Titanium Base Metals

Jae-Deuk Kim [1], **Siva Prasad Murugan** [2], **Seong-Woo Choi** [3], **Yutaka S. Sato** [4], **Jae-Keun Hong** [3], **Changwook Ji** [1], **Chang-Sub Kwak** [5] **and Yeong-Do Park** [6,*]

1   Advanced Forming Process R&D Group, Korea Institute of Industrial Technology, Ulsan 44413, Korea
2   LaSIE UMR CNRS 7356, La Rochelle Université, Avenue Michel Crépeau, 17000 La Rochelle, France
3   Metal Materials Division, Korea Institute of Materials Science, Changwon 51508, Korea
4   Department of Materials Processing, Graduate School of Engineering, Tohoku University, Sendai 980-8579, Japan
5   Fashion Tech Research Center, Industry Academic Cooperation Foundation, Catholic University of Daegu, Gyeongsan 38430, Korea
6   Department of Advanced Materials Engineering, Dong-Eui University, Busan 47340, Korea
*   Correspondence: ypark@deu.ac.kr; Tel.: +82-51-890-2290

Abstract: The mechanical properties of commercially pure titanium can further be improved through the grain refinement processes; however, welding fine-grained materials is challenging due to the grain coarsening in the weld area and hence the weakening of the mechanical properties locally. Meanwhile, friction stir welding is a promising process in which the metallurgical bonding is established through the solid-state mechanical mixing of materials to be welded; no studies have reported friction stir welding of the ultra-fine-grained commercial purity titanium to date. In this research, friction stir welding of fine-grained and ultra-fine-grained commercially pure titanium (1.58 and 0.66 μm, respectively) was conducted. The effect of the microstructural feature of base metals on the microstructural evolution of the stir zone and the feasibility of the friction stir welding process for those materials were discussed. It was found that the fraction of twin boundaries in ultra-fine-grained material was higher than in fine-grained material. It accelerated dynamic recrystallization and recovery in the stir zone, hence inducing the grain coarsening and the loss of ultra-fine-grained structure and character after welding.

1. Introduction

Commercially pure titanium (CP-Ti) is a silver-colored light metal with a hexagonal close-packed (HCP) crystal structure that is known as α-Ti stable below 883 °C [1]. Ti and its alloys have a high specific strength, corrosion resistance, and biocompatibility. Thus, it is a promising material for various industries of aeronautics, defense, biomedical, etc. The mechanical properties of titanium (Ti) and its alloys can further be improved through the grain refinement process, such as severe plastic deformation. The fine-grained and ultra-fine-grained Ti can be produced by several processes, such as equal channel angular processing, friction stir processing, cryogenic, cold and hot rolling, and so on [2–7]. In general, the fine-grained microstructure consists of grains with sizes in the order of 1 μm, while ultra-fine-grained with sizes less than 1 μm [8]. When the Ti material undergoes severe plastic deformation at the temperature below the β-transus, a dynamic recrystallization (DRX) occurs by fragmentation of the initial microstructure as well as a dynamic recovery (DRV; i.e., dislocation annihilation). As a result, fine equiaxed and elongated α

phases with high residual stress and strain represented by a high fraction of subgrains and subboundaries are produced [8].

Welding is an essential technique for assembling and manufacturing structural parts using materials in engineering applications; however, welding fine- and ultra-fine-grained material is a challenging issue as they are susceptible to recrystallization and grain growth. The recrystallization and grain growth in the weld area result in the elimination of the fine- and ultra-fine-grained structure and weaken the mechanical properties in the weld area. A few studies regarding the welding of fine-grained materials have been reported, such as diminishing (or even elimination) of the fine-grained structure, recrystallization and inexorable grain coarsening, and a consequent degradation of mechanical properties in the weld area [9,10]. Meanwhile, friction stir welding (FSW) is a promising alternative welding process for fine-grained materials, as it is a solid-state joining process [1]. FSW is conducted at the peak temperature of about half to three-quarters of the melting temperature of the material. It makes joints through the stirring of viscoplastic state material by means of the tool movement and a plastic flow by material softening via elevated temperature induced by the friction between the tool and material [8,11,12]; thus, the FSW could be the proper process for fine-grained material to avoid grain growth and weakening of the weld area. A few studies on the FSW of fine-grained material have been reported using low carbon steel, stainless steel, aluminum, copper, etc. [13–19]; however, to the authors' best knowledge, FSW of ultra-fine-grained CP-Ti has not been the topic of any research to date.

In this research, FSW of fine- and ultra-fine-grained CP-Ti was conducted. Firstly, the grain boundary character distribution (GBCD) of each base metal (BM) and stir zone (SZ) were analyzed to find out the effect of the microstructural feature of BM on the microstructural evolution of SZ using electron backscattered diffraction (EBSD) analysis. In the end, the feasibility of the FSW process to join fine- and ultra-fine-grained CP-Ti material was discussed.

2. Materials and Methods

2.1. Materials

The fine- and ultra-fine-grained CP-Ti sheets were obtained by cold rolling (at 25 °C) and cryogenic rolling (at −100 °C), respectively, from commercial grade 2 Ti alloy with an average grain size of 40 μm. The chemical composition and details of each rolling process history are given in Appendix A. As a result of 80% thickness reduction, the average grain size of fine- and ultra-fine-grained CP-Ti was about 1.5 and 0.66 μm, respectively.

2.2. Friction Stir Welding Parameters

The 1.0 mm thick fine- and ultra-fine-grained CP-Ti sheets were used as the BM in this research. The welding was conducted as a configuration of the lap joint of double sheets of each BM. A flat cylindrical type of cobalt alloy tool was used. The tool consisted of a flat shoulder and a smooth tapered pin with a circle end shape, as shown in Figure 1a. The welding tool had dimensions of 15 mm, 3.5–6.0 mm, and 1.7 mm for shoulder diameter, pin diameter, and pin length, respectively. The welding was conducted along the transverse direction (TD; i.e., WD), and perpendicular to the rolling direction (RD). The tool rotation speed and travel speed (same as welding speed) were given as 140 RPM and 60 mm/min, respectively. The welding tool was tilted 3° opposite to the welding direction, and the tool rotation direction was counterclockwise in this research. The *Z*-axis displacement control was adopted to control the tool plunging. The samples for the welding were fixed using a pneumatic Jig system and were shielded by an attachable local argon gas shielding system with a type of cap to avoid oxidation during the welding, as shown in Figure 1b. The lap joint welding of fine- and ultra-fine-grained BM was well conducted with none of the internal defects.
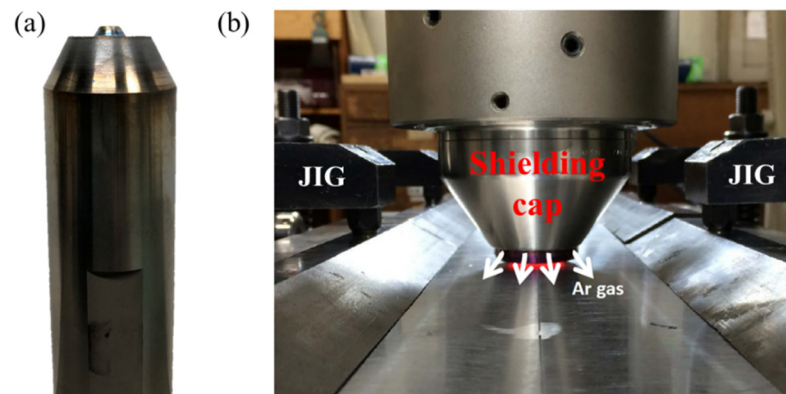
Figure 1. The photograph of (**a**) the tool used for friction stir welding in this experiment and (**b**) the pneumatic JIG and cap type local Ar shielding system.

2.3. Microstructure Characterization

The welded samples were cut as a cross-section specimen by a diamond wheel cutting and ground and polished mechanically till 0.04 μm colloidal silica. An EBSD analysis was conducted to investigate the microstructure and boundary analysis of interesting regions: the center of the cross-section of the BM and SZ. Jeol JSM-7001F (JEOL Ltd., Tokyo, Japan) and Oxford Instruments X-MAX (Oxford Instruments, Abingdon, UK) were used for the EBSD analysis. The step size of 0.003 and 0.015 μm were used for BM and SZ, respectively. A magnification of ×6000 and ×2000 were adopted for BM and SZ, respectively. The post-processing and analysis of the EBSD were performed using TSL orientation imaging microscopy (OIM) analysis software. The data of inverse pole figure (IPF), misorientation map and kernel average misorientation (KAM) map, etc., in each region, were obtained by using OIM analysis software (version 7.3.1., EDAX, Mahwah, NJ, USA). In this paper, low angle boundaries (LABs) were parted at 2–15°, and high angle boundaries (HABs) refer to a misorientation angle greater than 15° [8].

3. Results and Discussion

3.1. Base Metal Microstructure

Figure 2 shows the results of the EBSD analysis of the fine-grained BM and ultra-fine-grained BM. Despite the adoption of an extremely small step size, as mentioned in Section 2, due to the highly fine grains and high strain or dislocation density in the microstructure, the indexing rate of fine-grained BM and ultra-fine-grained BM was rated as 83.2 and 52.97%, respectively. The average grain size of fine-grained BM was measured as 1.58 ± 0.28 μm and that of ultra-fine-grained BM was 0.66 ± 0.28 μm.

For further understanding of the GBCD of fine-grained BM and ultra-fine-grained BM, the analysis of misorientation distribution was conducted, and the results are shown in Figure 3. The fraction of LABs and HABs were similar in fine-grained BM and ultra-fine-grained BM, as shown in Figure 3a,b. The major graphs in Figure 3c,d deal with the misorientation angle of 2 to 95°. It is notable that the fraction of LABs was measured as 50.8 and 53.6% in fine-grained BM and ultra-fine-grained BM, respectively. It can be said that the highly dense tangled dislocations are present in both BMs. The LABs could be considered subgrain and subgrain boundaries as they are formed by the arrangement of dislocations and make an orientation difference of less than or equal to 15° across the boundary [8]. The LABs in BM were formed by the severe plastic deformation at room and cryogenic temperatures. Those LABs are regarded as the indication of high imposed strain in the microstructure of BMs; thus, it is the major reason for the high level of KAM results in Figure 2b,d [8,20–27].
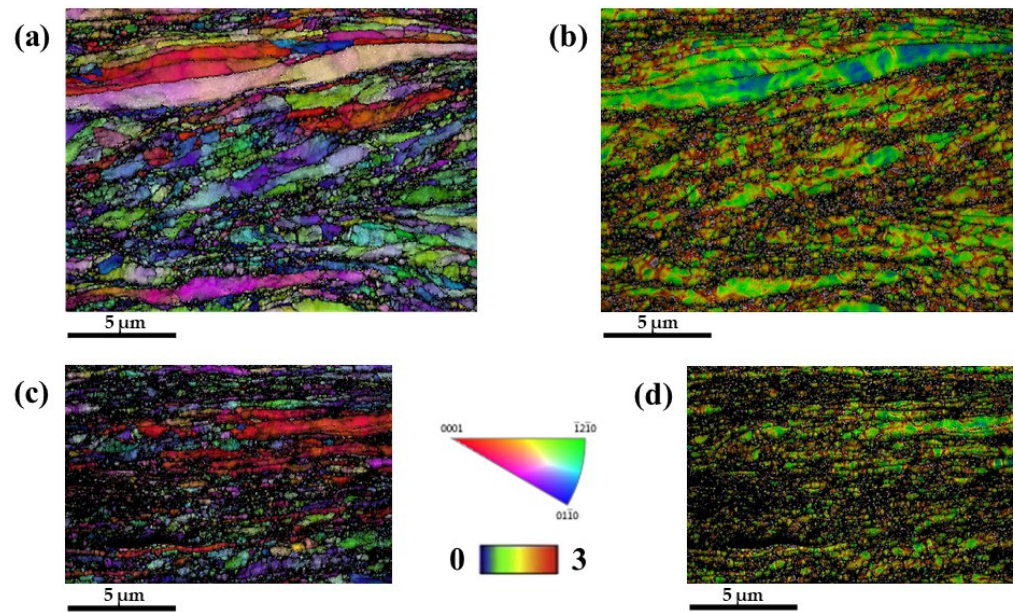
Figure 2. Microstructure of the BM of fine-grained and ultra-fine-grained CP-Ti characterized by using EBSD; IPF and KAM map of fine-grained BM are shown in (**a**,**b**), and those of ultra-fine-grained BM are shown in (**c**,**d**), respectively (the scales of figures are equal in here).
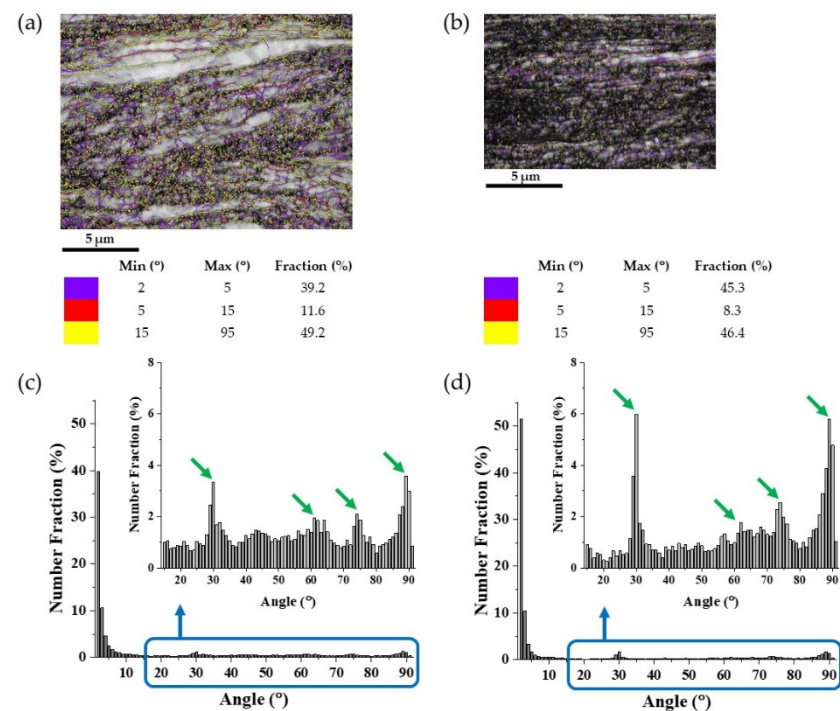

Figure 3. Boundary maps of (**a**) fine-grained BM and (**b**) ultra-fine-grained BM are shown with quantitative numerical values of GBCD of each. The misorientation angle distribution in (**c**) fine-grained BM and (**d**) ultra-fine-grained BM are plotted. The graphs show the misorientation angle ranges of 2 to 90°, and the inset graphs show the misorientation angles of 15 to 90° (enlarged plot of blue box areas).

Both IPF maps in Figure 2a,c show blue and green color grains, which are the fragmented fine grains because of severe plastic deformation by cold rolling and cryogenic rolling, respectively. The colors blue and green show that the basal plane of those grains is tilted from the normal direction (ND) to TD. In contrast, the red and purple color elongated

grains are the remnant elongated grains that are not yet fragmented but have highly dense internal crystallographic defects, as can be seen in the KAM maps in Figure 2b,d. Further, it can be found in KAM maps of each that the kernel misorientation deviation is highly complicated and differs among the grains, which are represented by yellow and red colors. The highly complicated and differed kernel misorientation means high imposed strain energy in the material. In other words, the material is metallurgically unstable. The metallurgical instability of the material here would be mainly caused by the dense dislocations and twins; it is reasonable to consider that it is possibly dominated by the twins because the CP-Ti is composed of only α-Ti phase with HCP crystal structure either at room temperature or at cryogenic temperature. Moreover, it has highly limited slip systems at cryogenic and room temperature [8,20–27].

Meanwhile, minor graphs inset above the major graphs in Figure 3c,d deal with 15 to 95°, also known as HABs. The fraction of HABs in fine-grained BM and ultra-fine-grained BM were measured as 49.2 and 46.4%, respectively. It is worthwhile to see the GBCD of HABs in CP-Ti because it has a limited number of independent slip systems and has low stacking fault energy (SFE); thus, twinning is prone to occur. The twinning resolves the strain when it is deformed physically at room and cryogenic temperatures. Under further strain, it acts as subboundaries; thus, twinned within it or split/fragmented [28–31]. This is the main mechanism for producing the fine- and ultra-fine-grained CP-Ti material by severe plastic deformation. The results of the HABs analysis revealed that four peaks exist (marked by green arrows) in both graphs, which show a similar trend that has peaks near 30°, 60°, 75°, and 90°. The GBCD of near 30°, 60°, and 90° is dominated by twin boundaries (TBs) and α/α boundary as listed in Table 1, but none of the references were found regarding the near 75°. The TBs were the result of severe plastic deformation at room and cryogenic temperatures as aforementioned [8,20–27]. At room temperature, a major deformation mechanism during rolling is a combination of prism<a> slip + pyramidal<a> slip and tensile + compression twinning as well. At cryogenic temperature, on the other hand, the mechanism would be changed to the tensile and compression twinning due to the lesser CRSS of twinning than prism<a> slip + pyramidal<a> slip. As a result, the ultra-fine-grained BM showed an almost doubled 30° and 90° misorientation angle than fine-grained BM in fraction, and those are mainly considered the TBs. These TBs are also regarded as the indication of high imposed strain in the microstructure of both BMs, similar to the LABs, because it is a result of severe deformation and possibly acts as subgrains and subgrain boundaries in the microstructure [8,20–26].

Table 1. Featured high angle boundary characters of CP-Ti of near 30°, 60°, 75°, and 90° [8,21–27].

Specific Angle	30 ± 5°	60 ± 5°	75 ± 5°	90 ± 5°
Featured high-angle boundary character	{11-22} compression twin <-1100> tensile twin	{1122} compression twin <-12-10> compression twin <11-20> α/α boundary <-10-7 17 3> α/α boundary <-10 5 5 -3> α/α boundary <-1100> compression twin	-	{101-2} tensile twin <7-17 10 0> α/α boundary <-12-10> tensile twin

3.2. Stir Zone Microstructure

Figure 4 shows the results of the EBSD analysis of the fine-grained SZ and ultra-fine-grained SZ. Owing to the recrystallization and grain growth after the FSW, the indexing rate of fine-grained SZ and ultra-fine-grained SZ was more than 95%. The average grain size of fine-grained SZ was measured as 2.34 ± 1.70 μm and that of ultra-fine-grained BM was 3.19 ± 2.31 μm. Ultra-fine-grained SZ is coarser than fine-grained SZ, despite

the ultra-fine-grained BM showing a smaller grain size than fine-grained BM as shown in Figure 4a,c. On the contrary, the level of KAM is higher in fine-grained BM than in ultra-fine-grained BM, as seen in Figure 4b,d. The comparison of microstructure analysis results of fine-grained SZ and ultra-fine-grained SZ showed the opposite tendency to that of the fine-grained BM and ultra-fine-grained BM. In the next section, the GBCD analysis results are discussed to find out the reason for this phenomenon deeply.
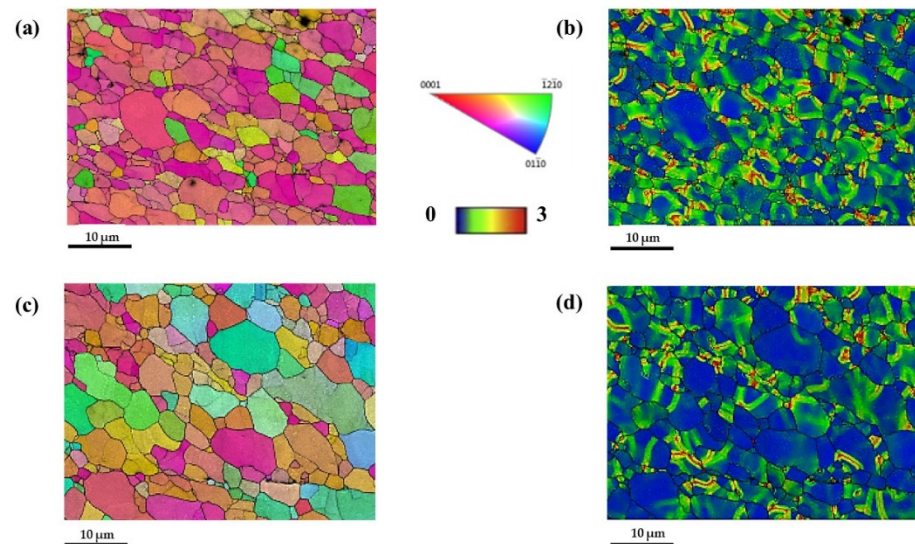

Figure 4. Microstructure of the SZ of fine-grained and ultra-fine-grained CP-Ti characterized by using EBSD; IPF and KAM map of fine-grained SZ are shown in (**a**,**b**), and those of ultra-fine-grained SZ are shown in (**c**,**d**), respectively (the scales of figures are equal in here).

4. Discussion

4.1. Evolution of Grain Boundary Character Distribution: Base Metal to Stir Zone

Before discussing in-depth, we must define the dominant microstructural evolution mechanism in SZ. There were no serrated boundaries observed, as shown in Figure 4a,c; thus, it can be said that the peak temperature during welding was below the β-transus temperature [8]; therefore, it can be thought that the $\alpha \to \beta \to \alpha$ phase transformation was absent during welding, and hence the microstructural evolution within both SZ was dominated by the DRX and DRV [8,20,22,23,32,33]. The driving force for the DRX during FSW would be the heat generated and strain energy by the tool rotation and high imposed internal strain energy by a high fraction of LABs and TBs, which could act as subgrains and subgrain boundaries in the initial microstructure.

Meanwhile, the fraction of LABs was similar in fine-grained BM and ultra-fine-grained BM as shown in Figure 3a,b, yet the fraction of TBs highly differed in fine-grained BM and ultra-fine-grained BM. Ultra-fine-grained BM showed an almost doubled TBs fraction than fine-grained BM, as shown in Figure 3c,d. Further, the heat input and given load were the same in both SZs because the same process parameters were adopted, as mentioned in Section 2; thus, it is reasonable to consider that the amount of TBs fraction in BM would be the key to understanding the reason for microstructural evolution differences in fine-grained and ultra-fine-grained material.

The misorientation angle distribution in BM and SZ of both fine-grained and ultra-fine-grained are shown in Figure 5a,b, and it can be seen that the HABs fraction was 10% higher in ultra-fine-grained SZ than fine-grained SZ. To find out the reason for the higher HABs fraction, the peaks of misorientation angles related to TBs are highlighted by green arrows in Figure 5c,d. It is notable that the fraction of near 60° and 90° disappeared after the FSW in both cases, and near 30° also decreased in the case of ultra-fine-grained. During the FSW, tensile and compression load would be given to the material in a viscoplastic solid state [34] under the temperature below the β-transus; therefore, when the tool passes

through the material, the high fraction of TBs within one grain would accelerate the fragmentation of original grains since it acts as a thin substructure similar to the lath domain structure [20–27]. In other words, the ultra-fine-grained BM could have a higher chance of fragmentation of quasi-lath grains along the TBs and have more DRX sites by consuming the TBs. Misorientation angle plots of near 30°, 60°, and 90° were sorted from BM and SZ of both samples and plotted in Figure 5. It was found that the boundaries related to misorientation angles of 60° and 90° disappeared after the FSW; thus, the ultra-fine-grained BM had a higher chance of DRX in the early stage (*induced by the higher fraction of TBs*) and grain growth of DRXed grains, hence, it had enough time for grain coarsening through the consuming of smaller grains nearby. Ahn et al. [35] reported that the grain growth of CP-Ti is very fast and inexorable once it starts. Consequently, ultra-fine-grained SZ revealed the equiaxed morphology and larger grain sizes than the fine-grained SZ despite the finer microstructure in BM.
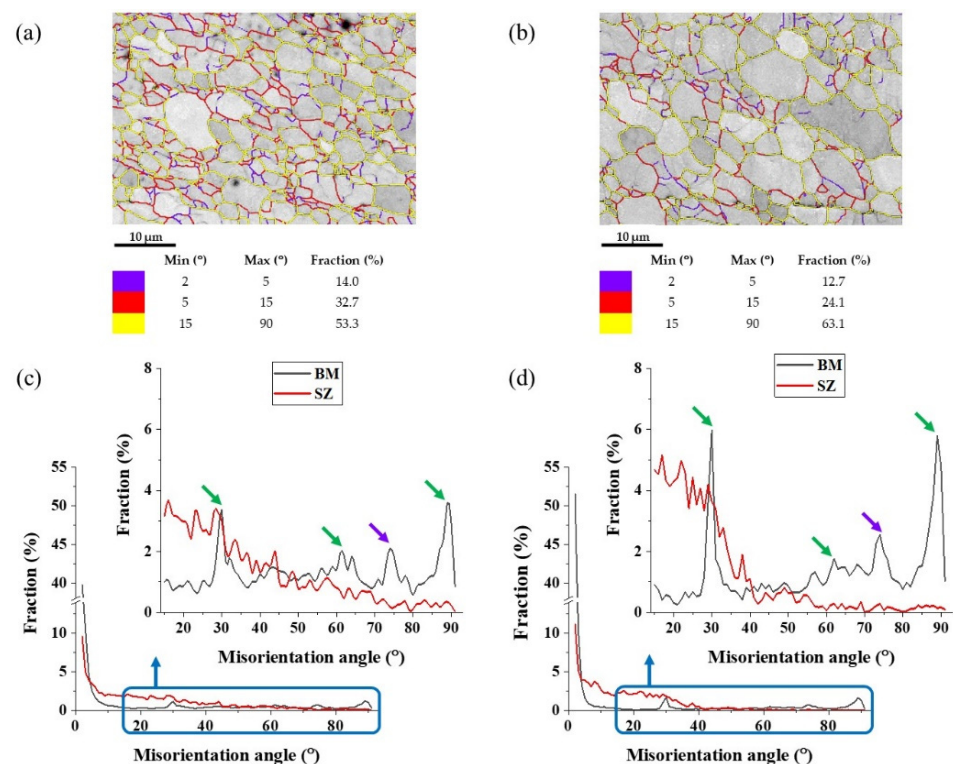

Figure 5. Boundary maps of (**a**) fine-grained SZ and (**b**)ultra-fine-grained SZ are shown with quantitative numerical values of GBCD of each. Misorientation angle distribution in BM and SZ of (**c**) fine-grained and (**d**) ultra-fine-grained. The graphs show the misorientation angle ranges of 2 to 90°, and the inset graphs show the misorientation angles of 15 to 90° (enlarged plot of blue box areas). The black lines and red lines represent BM and SZ, respectively.

The fraction of 30° TBs was still high in both samples, as shown in Figures 5 and 6. It might be due to the given tensile and compression strain to the viscoplastic state material during the FSW [34]. It can be assumed that the 30° TBs formed within the newly formed DRXed and DRVed grains, and the KAM map shows evidence of that, as shown in Figure 4b,d. Meanwhile, the peaks near 75° in both BM, which had unrevealed in Section 3.2, had disappeared in both SZ (highlighted by purple arrows in Figure 5). It can be assumed to be related to the pile of dense dislocations rearranged and coalescence during severe plastic deformation and eliminated during FSW by DRV (i.e., dislocation annihilation) as well as DRX [8].
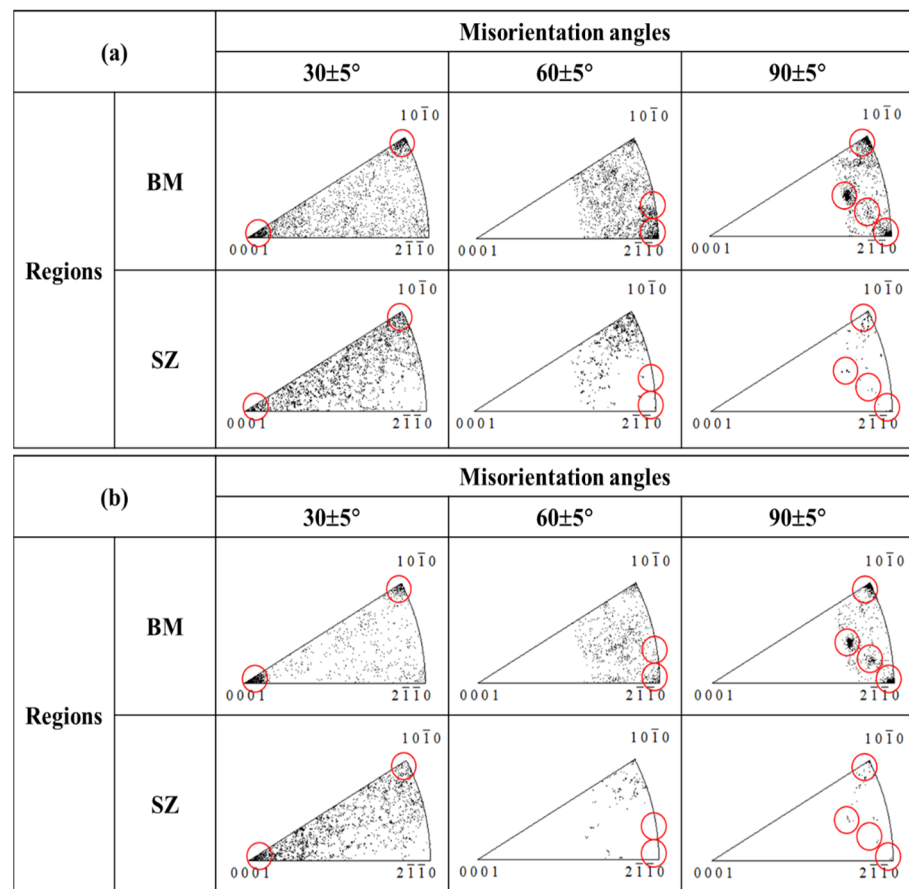
Figure 6. Misorientation angle plots sorted from BM and SZ of (**a**) fine-grained CP-Ti and (**b**) ultra-fine-grained CP-Ti. Angles of 30, 60, and 90°, which are related to TBs evaluated both in BM and SZ.

The ultra-fine-grained SZ loses its advantageous microstructure and character after the FSW. Further, it has a larger grain size of 1.36 times than the fine-grained SZ. This phenomenon is mainly due to the early DRX and grain growth via more DRX sites *induced by high TBs fraction* in ultra-fine-grained BM, plus the nature of fast grain growth of CP-Ti due to low thermal stability. The deformation TBs are special boundaries possessing high mobility that allow them to grow out of the system, especially in nanocrystalline and ultra-fine-grained microstructure [36]. Moreover, TBs play a key role in changing local grain orientation and dissociating boundaries of fine grains, resulting in effective grain growth [37]. The mobility of twins works via the atomic shuffling mechanism or through the propagation of twin partial dislocations on parallel twin planes [38].

4.2. Feasiliblity of Friction Stir Welding on Fine-Grained and Ultra-Fine-Grained CP-Ti Material

As mentioned in previous sections, fine-grained and ultra-fine-grained CP-Ti should be welded when applied to any industrial applications. The FSW was chosen in this research to avoid the loss of fine-grained and ultra-fine-grained structure and its character. From a view of grain size change before and after the welding, fine-grained SZ showed grain growth of 1.48 times compared to fine-grained BM and it preserved the fine-grained microstructure to a degree. In contrast, ultra-fine-grained SZ showed considerable grain growth and it was about 4.8 times of ultra-fine-grained BM. So, it can be summarized that the character of ultra-fine-grained CP-Ti with a high fraction of TBs cannot be sustainable even if the FSW is used, even with a peak temperature of less than the β-transus. The formation of TBs during the severe plastic deformation process should be carefully designed accordingly to obtain less fraction of deformation TBs and thus suppress the grain mobility and grain coarsening. It can be achieved through optimizing the process parameters used in the severe plastic

deformation procedure, such as the temperature, number of passes, annealing temperature, external magnetic field, etc. [39–42]. Otherwise, the use of processes with less heat input with faster cooling (e.g., laser and laser hybrid welding) for welding ultra-fine-grained CP-Ti with a high fraction of TBs, etc., are viable solutions. Further, it would rather be advantageous to use fine-grained CP-Ti when considering the manufacturing time and cost for material and the subsequent grain coarsening induced by the high fraction of TBs.

5. Conclusions

In this research, friction stir welding of fine-grained and ultra-fine-grained CP-Ti with a grain size of 1.58 and 0.66 μm, respectively, was conducted. The effect of the microstructural feature of the base metal on the microstructural evolution of the stir zone was then discussed. Finally, the feasibility of the friction stir welding process for those materials was conferred. The conclusions from this research are as follows:

- Differences in grain boundary character distribution were observed in fine-grained and ultra-fine-grained titanium base metal owing to the different rolling temperatures of cold and cryogenic rolling.
- Observation of differences in microstructural evolution in stir zones were due to grain boundary character distribution differences in each base metal, primarily the fraction of twin boundaries.
- The grain coarsening in the stir zone of ultra-fine-grained commercially pure titanium was induced by a high fraction of twin boundaries and was not able to maintain ultra-fine-grained structures and characters.
- The more the fraction of twin boundaries in base metal, the more the dynamic recrystallization accelerated and subsequently coarsened, and equiaxed grains were formed in the stir zone
- The formation of TBs should be carefully controlled when considering the welding and joining of ultra-fine-grained commercially pure titanium for any application.

Author Contributions: Conceptualization, J.-D.K., S.P.M. and Y.-D.P.; methodology, J.-D.K. and S.P.M.; software, J.-D.K. and S.-W.C.; validation, J.-D.K. and S.P.M.; formal analysis, J.-D.K. and S.P.M.; investigation, J.-D.K., S.P.M. and Y.-D.P.; resources, Y.S.S.; data curation, J.-D.K. and S.P.M.; writing—original draft preparation, J.-D.K.; writing—review and editing, J.-D.K., S.P.M., S.-W.C., Y.S.S., J.-K.H., C.J., C.-S.K. and Y.-D.P.; visualization, J.-D.K. and S.P.M.; supervision, Y.-D.P.; project administration, J.-K.H., J.-D.K. and Y.-D.P.; funding acquisition, C.-S.K., J.-K.H. and Y.-D.P. All authors have read and agreed to the published version of the manuscript.

Institutional Review Board Statement: Not applicable.

Informed Consent Statement: Not applicable.

Data Availability Statement: Data sharing is not applicable.

Conflicts of Interest: The authors declare no conflict of interest.

Nomenclature

BM	base metal
CP-Ti	commercially pure titanium
DRV	dynamic recovery
DRX	dynamic recrystallization
EBSD	electron backscattered diffraction
FSW	friction stir welding
GBCD	grain boundary character distribution
HAB	high angle boundary

HCP	hexagonal close-packed
IPF	inverse pole figure
KAM	kernel average misorientation
LAB	low angle boundary
ND	normal direction
RD	rolling direction
SFE	stacking fault energy
SZ	stir zone
TB	twin boundary
TD	transverse direction
Ti	titanium
WD	welding direction

Appendix A

The chemical composition and details of each rolling process history are shown in Figure A1a. The average grain size of the initial microstructure was measured at approximately 40 μm, as shown in Figure A1b. The total reduction in thickness was about 78% in both rolling processes, which are shown in Figure A1c,d. The entire process of fabricating the fine-grained and ultra-fine-grained CP-Ti base metal was conducted by the Korea Institute of Materials Science (KIMS).
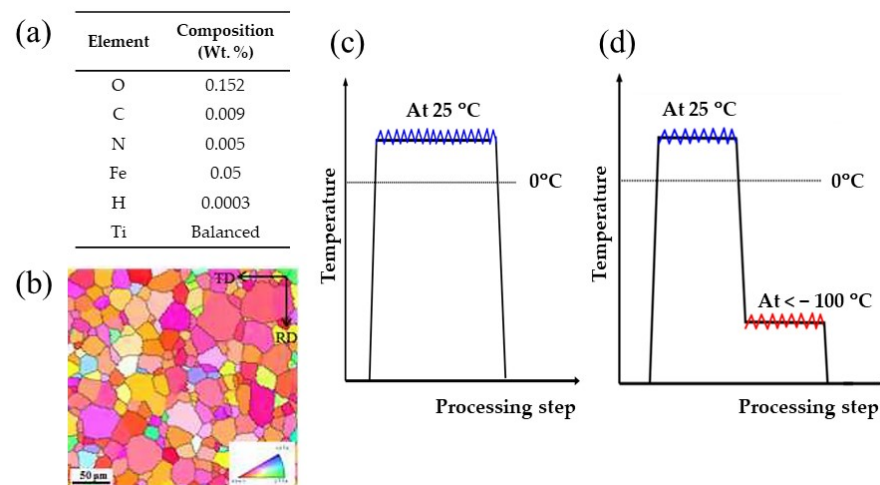

Figure A1. (**a**) Chemical composition of the material used. (**b**) Initial microstructure of CP-Ti Gr.2 before the rolling. (**c,d**) shows the rolling history of cold rolling and cryogenic rolling; total reduction in area was about 78% in both.

References

1. Kim, J.D.; Jin, E.G.; Murugan, S.P.; Park, Y.D. Recent Advances in Friction-Stir Welding Process and Microstructural Investigation of Friction Stir Welded Pure Titanium. *J. Weld. Join.* **2017**, *35*, 6–15. [CrossRef]
2. Valiev, R.Z.; Estrin, Y.; Horita, Z.; Langdon, T.G.; Zehetbauer, M.J.; Zhu, Y. Producing Bulk Ultrafine-Grained Materials by Severe Plastic Deformation: Ten Years Later. *JOM* **2016**, *68*, 1216–1226. [CrossRef]
3. Gholinia, A.; Humphreys, F.J.; Prangnell, P.B. Production of Ultra-Fine Grain Microstructures in Al-Mg Alloys by Coventional Rolling. *Acta Mater.* **2002**, *50*, 4461–4476. [CrossRef]
4. Ko, Y.G.; Shin, D.H.; Park, K.T.; Lee, C.S. An Analysis of the Strain Hardening Behavior of Ultra-Fine Grain Pure Titanium. *Scr. Mater.* **2006**, *54*, 1785–1789. [CrossRef]
5. Sanosh, K.P.; Balakrishnan, A.; Francis, L.; Kim, T.N. Vickers and Knoop Micro-Hardness Behavior of Coarse-and Ultrafine-Grained Titanium. *J. Mater. Sci. Technol.* **2010**, *26*, 904–907. [CrossRef]
6. Momeni, A.; Abbasi, S.M. Repetitive Thermomechanical Processing towards Ultra Fine Grain Structure in 301, 304 and 304L Stainless Steels. *J. Mater. Sci. Technol.* **2011**, *27*, 338–343. [CrossRef]
7. Bézi, Z.; Krállics, G.; El-Tahawy, M.; Pekker, P.; Gubicza, J. Processing of Ultrafine-Grained Titanium with High Strength and Good Ductility by a Combination of Multiple Forging and Rolling. *Mater. Sci. Eng. A* **2017**, *688*, 210–217. [CrossRef]

8. Kim, J.D.; Murugan, S.P.; Kim, J.W.; Chun, C.K.; Kim, S.W.; Hong, J.K.; Choi, S.W.; Ji, C.W.; Kim, J.U.; Park, Y.D. Do α/β Phase Transformation and Dynamic Recrystallization Induced Microstructure Development in Fine-Grained Ti-6Al-4V Friction Stir Weld. *Mater. Charact.* **2021**, *178*, 111300. [CrossRef]

9. Gao, M.; Zeng, X.; Hu, Q.; Yan, J. Laser-TIG Hybrid Welding of Ultra-Fine Grained Steel. *J. Mater. Process. Technol.* **2009**, *209*, 785–791. [CrossRef]

10. Tian, Z.; Peng, Y. Welding of Ultra-Fine Grained Steels. In *Ultra-Fine Grained Steels*; Springer: Berlin, Heidelberg, Germany, 2009; pp. 494–566. ISBN 978-3-540-77230-9. [CrossRef]

11. Arora, K.S.; Pandey, S.; Schaper, M.; Kumar, R. Microstructure Evolution during Friction Stir Welding of Aluminum Alloy AA2219. *J. Mater. Sci. Technol.* **2010**, *26*, 747–753. [CrossRef]

12. Mironov, S.; Sato, Y.S.; Kokawa, H. Friction-Stir Welding and Processing of Ti-6Al-4V Titanium Alloy: A Review. *J. Mater. Sci. Technol.* **2018**, *34*, 58–72. [CrossRef]

13. Fujii, H.; Ueji, R.; Takada, Y.; Kitahara, H.; Tsuji, N.; Nakata, K.; Nogi, K. Friction Stir Welding of Ultrafine Grained Interstitial Free Steels. *Mater. Trans.* **2006**, *47*, 239–242. [CrossRef]

14. Ueji, R.; Fujii, H.; Cui, L.; Nishioka, A.; Kunishige, K.; Nogi, K. Friction Stir Welding of Ultrafine Grained Plain Low-Carbon Steel Formed by the Martensite Process. *Mater. Sci. Eng. A* **2006**, *423*, 324–330. [CrossRef]

15. Malopheyev, S.; Mironov, S.; Kulitskiy, V.; Kaibyshev, R. Friction-Stir Welding of Ultra-Fine Grained Sheets of Al-Mg-Sc-Zr Alloy. *Mater. Sci. Eng. A* **2015**, *624*, 132–139. [CrossRef]

16. Sabooni, S.; Karimzadeh, F.; Enayati, M.H.; Ngan, A.H.W. Recrystallisation Mechanism during Friction Stir Welding of Ultrafine- and Coarse-Grained AISI 304L Stainless Steel. *Sci. Technol. Weld. Join.* **2016**, *21*, 287–294. [CrossRef]

17. Wang, Y.F.; An, J.; Yin, K.; Wang, M.S.; Li, Y.S.; Huang, C.X. Ultrafine-Grained Microstructure and Improved Mechanical Behaviors of Friction Stir Welded Cu and Cu-30Zn Joints. *Acta Met. Sin. (Engl. Lett.)* **2018**, *31*, 878–886. [CrossRef]

18. Orłowska, M.; Brynk, T.; Hütter, A.; Goliński, J.; Enzinger, N.; Olejnik, L.; Lewandowska, M. Similar and Dissimilar Welds of Ultrafine Grained Aluminium Obtained by Friction Stir Welding. *Mater. Sci. Eng. A* **2020**, *777*, 139076. [CrossRef]

19. Orłowska, M.; Olejnik, L.; Campanella, D.; Buffa, G.; Morawiński, Ł.; Fratini, L.; Lewandowska, M. Application of Linear Friction Welding for Joining Ultrafine Grained Aluminium. *J. Manuf. Process.* **2020**, *56*, 540–549. [CrossRef]

20. Zherebtsov, S.V.; Dyakonov, G.S.; Salem, A.A.; Sokolenko, V.I.; Salishchev, G.A.; Semiatin, S.L. Formation of Nanostructures in Commercial-Purity Titanium via Cryorolling. *Acta Mater.* **2013**, *61*, 1167–1178. [CrossRef]

21. Won, J.W.; Lee, T.; Hong, S.G.; Lee, Y.; Lee, J.H.; Lee, C.S. Role of Deformation Twins in Static Recrystallization Kinetics of High-Purity Alpha Titanium. *Metall. Mater. Int.* **2016**, *22*, 1041–1048. [CrossRef]

22. Won, J.W.; Lee, J.H.; Jeong, J.S.; Choi, S.W.; Lee, D.J.; Hong, J.K.; Hyun, Y.T. High Strength and Ductility of Pure Titanium via Twin-Structure Control Using Cryogenic Deformation. *Scr. Mater.* **2020**, *178*, 94–98. [CrossRef]

23. Choi, S.W.; Jeong, J.S.; Won, J.W.; Hong, J.K.; Choi, Y.S. Grade-4 Commercially Pure Titanium with Ultrahigh Strength Achieved by Twinning-Induced Grain Refinement through Cryogenic Deformation. *J. Mater. Sci. Technol.* **2021**, *66*, 193–201. [CrossRef]

24. Kim, G.; Shams, S.A.A.; Kim, J.N.; Won, J.W.; Choi, S.W.; Hong, J.K.; Lee, C.S. Enhancing Low-Cycle Fatigue Life of Commercially-Pure Ti by Deformation at Cryogenic Temperature. *Mater. Sci. Eng. A* **2021**, *803*, 140698. [CrossRef]

25. Choi, S.W.; Li, C.L.; Won, J.W.; Yeom, J.T.; Choi, Y.S.; Hong, J.K. Deformation Heterogeneity and Its Effect on Recrystallization Behavior in Commercially Pure Titanium: Comparative Study on Initial Microstructures. *Mater. Sci. Eng. A* **2019**, *764*, 138211. [CrossRef]

26. Won, J.W.; Choi, S.W.; Yeom, J.T.; Hyun, Y.T.; Lee, C.S.; Park, S.H. Anisotropic Twinning and Slip Behaviors and Their Relative Activities in Rolled Alpha-Phase Titanium. *Mater. Sci. Eng. A* **2017**, *698*, 54–62. [CrossRef]

27. Kelly, M.N.; Glowinski, K.; Nuhfer, N.T.; Rohrer, G.S. The Five Parameter Grain Boundary Character Distribution of α-Ti Determined from Three-Dimensional Orientation Data. *Acta Mater.* **2016**, *111*, 22–30. [CrossRef]

28. Mironov, S.; Sato, Y.S.; Kokawa, H. Development of Grain Structure during Friction Stir Welding of Pure Titanium. *Acta Mater.* **2009**, *57*, 4519–4528. [CrossRef]

29. Svensson, L.E.; Karlsson, L.; Larsson, H.; Karlsson, B.; Fazzini, M.; Karlsson, J. Microstructure and Mechanical Properties of Friction Stir Welded Aluminium Alloys with Special Reference to AA 5083 and AA 6082. *Sci. Technol. Weld. Join.* **2000**, *5*, 285–296. [CrossRef]

30. Asadi, E.; Asle Zaeem, M. The Anisotropy of Hexagonal Close-Packed and Liquid Interface Free Energy Using Molecular Dynamics Simulations Based on Modified Embedded-Atom Method. *Acta Mater.* **2016**, *107*, 337–344. [CrossRef]

31. Xu, N.; Song, Q.; Bao, Y.; Jiang, Y.; Shen, J.; Cao, X. Twinning-Induced Mechanical Properties' Modification of CP-Ti by Friction Stir Welding Associated with Simultaneous Backward Cooling. *Sci. Technol. Weld. Join.* **2017**, *22*, 610–616. [CrossRef]

32. Bozzolo, N.; Dewobroto, N.; Wenk, H.R.; Wagner, F. Microstructure and Microtexture of Highly Cold-Rolled Commercially Pure Titanium. *J. Mater. Sci.* **2007**, *42*, 2405–2416. [CrossRef]

33. Chao, Q.; Beladi, H.; Sabirov, I.; Hodgson, P.D. Deformation Behaviour of a Commercial Pure Titanium Alloy during Hot Compression Testing. *Mater. Sci. Forum* **2014**, *773–774*, 281–286. [CrossRef]

34. Nandan, R.; Lienert, T.J.; DebRoy, T. Toward Reliable Calculations of Heat and Plastic Flow during Friction Stir Welding of Ti-6Al-4V Alloy. *Int. J. Mater. Res.* **2008**, *99*, 434–444. [CrossRef]

35. Ahn, S.H.; Chun, Y.B.; Yu, S.H.; Kim, K.H.; Hwang, S.K. Microstructural Refinement and Deformation Mode of Ti under Cryogenic Channel Die Compression. *Mater. Sci. Eng. A* **2010**, *528*, 165–171. [CrossRef]

36.   Brons, J.G.; Thompson, G.B. A Comparison of Grain Boundary Evolution during Grain Growth in Fcc Metals. *Acta Mater.* **2013**, *61*, 3936–3944. [CrossRef]

37.   Luo, X.M.; Zhu, X.F.; Zhang, G.P. Nanotwin-Assisted Grain Growth in Nanocrystalline Gold Films under Cyclic Loading. *Nat. Commun.* **2014**, *5*, 3021. [CrossRef]

38.   Prasad, K.E.; Ramesh, K.T. In-Situ Observations and Quantification of Twin Boundary Mobility in Polycrystalline Magnesium. *Mater. Sci. Eng. A* **2014**, *617*, 121–126. [CrossRef]

39.   Molodov, D.A.; Konijnenberg, P.J. Grain Boundary and Grain Structure Control through Application of a High Magnetic Field. *Scr. Mater.* **2006**, *54*, 977–981. [CrossRef]

40.   Wang, Y.; He, W.; Liu, N.; Chapuis, A.; Luan, B.; Liu, Q. Effect of Pre-Annealing Deformation on the Recrystallized Texture and Grain Boundary Misorientation in Commercial Pure Titanium. *Mater. Charact.* **2018**, *136*, 1–11. [CrossRef]

41.   Frydrych, K.; Kowalczyk-Gajewska, K. Microstructure Evolution in Cold-Rolled Pure Titanium: Modeling by the Three-Scale Crystal Plasticity Approach Accounting for Twinning. *Metall. Mater. Trans. A* **2018**, *49*, 3610–3623. [CrossRef]

42.   Zherebtsov, S.V.; Dyakonov, G.S.; Salem, A.A.; Malysheva, S.P.; Salishchev, G.A.; Semiatin, S.L. Evolution of Grain and Subgrain Structure during Cold Rolling of Commercial-Purity Titanium. *Mater. Sci. Eng. A* **2011**, *528*, 3474–3479. [CrossRef]